



THE UNIVERSITY *of* EDINBURGH

Edinburgh Research Explorer

Structural basis of Mcm2–7 replicative helicase loading by ORC–Cdc6 and Cdt1

Citation for published version:

Yuan, Z, Riera, A, Bai, L, Sun, J, Nandi, S, Spanos, C, Chen, ZA, Barbon, M, Rappsilber, J, Stillman, B, Speck, C & Li, H 2017, 'Structural basis of Mcm2–7 replicative helicase loading by ORC–Cdc6 and Cdt1' Nature Structural & Molecular Biology. DOI: 10.1038/nsmb.3372

Digital Object Identifier (DOI):

[10.1038/nsmb.3372](https://doi.org/10.1038/nsmb.3372)

Link:

[Link to publication record in Edinburgh Research Explorer](#)

Document Version:

Peer reviewed version

Published In:

Nature Structural & Molecular Biology

General rights

Copyright for the publications made accessible via the Edinburgh Research Explorer is retained by the author(s) and / or other copyright owners and it is a condition of accessing these publications that users recognise and abide by the legal requirements associated with these rights.

Take down policy

The University of Edinburgh has made every reasonable effort to ensure that Edinburgh Research Explorer content complies with UK legislation. If you believe that the public display of this file breaches copyright please contact openaccess@ed.ac.uk providing details, and we will remove access to the work immediately and investigate your claim.



30 **Abstract**

31

32 To start DNA replication, the Origin Recognition Complex (ORC) and Cdc6 load a Mcm2-7
33 double hexamer onto DNA. Without ATP hydrolysis, ORC-Cdc6 recruits one Cdt1-bound
34 Mcm2-7 hexamer, forming an ORC-Cdc6-Cdt1-Mcm2-7 (OCCM) helicase loading intermediate.
35 Here we report a 3.9Å structure of the OCCM on DNA. Flexible Mcm2-7 winged-helix domains
36 (WHD) engage ORC-Cdc6. A three-domain Cdt1 configuration embraces Mcm2, Mcm4, and
37 Mcm6, nearly half of the hexamer. The Cdt1 C-terminal domain extends to the Mcm6 WHD,
38 which binds Orc4 WHD. DNA passes through the ORC-Cdc6 and Mcm2-7 rings. Origin DNA
39 interaction is mediated by an α -helix in Orc4 and positively charged loops in Orc2 and Cdc6.
40 The Mcm2-7 C-tier AAA+ ring is topologically closed by a Mcm5 loop that embraces Mcm2,
41 but the N-tier ring Mcm2-Mcm5 interface remains open. This structure suggests loading
42 mechanics of the first Cdt1-bound Mcm2-7 hexamer by ORC-Cdc6.

43

44 INTRODUCTION

45

46 The *S. cerevisiae* Origin Recognition Complex (ORC) is an ATPase complex composed of Orc1-
47 6¹⁻³. The composition and architecture of ORC is conserved in all eukaryotes⁴. Low resolution
48 electron microscopy (EM) showed that the six subunits are arranged into a crescent in the order
49 of Orc1-Orc4-Orc5-Orc3-Orc2, with Orc6 binding to Orc2/Orc3^{5,6}. This architecture is
50 confirmed by a recent crystal structure of an inactive *Drosophila* ORC (DmORC)⁷. This
51 DmORC core is a notched two-tiered ring composed of the N-tier ring of five AAA+ domains
52 and the C-tier ring of five winged helix (WH) domains of Orc1-5. Because the DmOrc1 AAA+
53 domain blocks the putative central DNA binding channel in the auto-inhibited conformation⁷,
54 the configuration of an active ORC has been unknown. The budding yeast ORC binds the
55 replication origins throughout the cell division cycle¹, but they are “licensed” during the G1
56 phase⁸. An early step is the binding of initiation factor Cdc6 to DNA-bound ORC to form the
57 ORC-Cdc6-DNA complex⁹. EM has shown that Cdc6 closes a gap in the crescent-shaped ORC
58 to form a ring^{9,10} and apparently activates a molecular switch in ORC, converting it from an
59 origin DNA binder to an active Mcm2-7 loader^{6,9}. However, the physical nature of the molecular
60 switch is currently unknown due to the lack of a high-resolution structure of ORC-Cdc6 on
61 DNA.

62

63 The next steps involve the sequential recruitment onto the origin DNA of two Cdt1-bound
64 hexamers of Mcm2-7 by ORC-Cdc6 to form a Mcm2-7 double-hexamer (D-H) that forms part of
65 the pre-Replicative Complex (pre-RC)^{8,11}. *In vitro* reactions using purified components have
66 demonstrated that a high salt-stable Mcm2-7 D-H is loaded on DNA in an ATP dependent
67 manner^{12,13}. Each hexamer within the D-H is assembled in a way that their respective Mcm3 and
68 Mcm6 subunits face each other, as revealed by EM of Maltose Binding Protein (MBP) tagged D-
69 H as well as a 3.8 Å resolution cryo-EM structure^{14,15}. The Mcm2-7 double-hexamer has a
70 central channel that is wide enough for passage of double stranded DNA, in agreement with
71 biochemical findings^{12,13}. Because the two Mcm2-7 hexamers are twisted relative to each other,
72 it was speculated that within the interface between the two hexamers an inflection point of the
73 DNA path is created, possibly promoting melting of the double stranded DNA when the helicase
74 becomes activated in S phase¹⁴. At the G1-S transition, the inactive D-H is converted into an
75 active replicative helicase that consists of a Mcm2-7 hexamer bound to Cdc45 and the four-
76 subunit GINS complex, called the CMG^{16,17}. Disruption of the Mcm2-7 D-H and assembly of
77 CMG require activation by the Dbf4-Cdc7 protein kinase (DDK) and Cyclin-Dependent Kinase
78 (CDK; Clb5-Cdc28), which phosphorylate some of the pre-RC components, such as Mcm2-7
79 subunits and accessory loading proteins Sld2 and Sld3^{1,8,18-26}. Subsequently, primase and DNA
80 polymerases load, along with many other replication factors, to form the replisome that executes
81 DNA synthesis^{27,28}.

82

83 The two Mcm2-7 hexamers are loaded on DNA sequentially^{15,29,30}. In the presence of ATP γ S,
84 ORC-Cdc6 loads the first Mcm2-7 hexamer on DNA, forming an ORC-Cdc6-Cdt1-Mcm2-7
85 intermediate (OCCM)³¹. Then ATP hydrolysis is triggered and Cdt1 is released, which leads to
86 the formation of the ORC-Cdc6-Mcm2-7 (OCM) complex^{30,32-34}. A time course analysis
87 suggests that it is the OCM that loads the second Cdt1-bound Mcm2-7 to form an ORC-Cdc6-
88 Mcm2-7-Mcm2-7 (OCMM) complex prior to Mcm2-7 D-H formation^{15,30,35}. *In vivo* evidence

89 suggests that ATP hydrolysis by Cdc6 causes the separation of the D-H from ORC-Cdc6³⁶. In
90 this work, we describe a 3.9 Å resolution cryo-EM structure of the 1.1-MDa 14-protein OCCM
91 complex on DNA and interactions between individual proteins using mass spectrometry. The
92 structure revealed how ORC-Cdc6 recognizes origin DNA and how this complex recruits the
93 first Cdt1-bound Mcm2-7 hexamer, thereby illuminating a crucial step in eukaryotic DNA
94 replication initiation.

95

96 RESULTS

97 Overall structure of the OCCM-DNA complex

98 We prepared the OCCM complexes in the presence of ATP γ S from purified proteins on a
99 replication origin containing plasmid attached to magnetic beads. Upon DNaseI treatment the
100 OCCM samples were released from the beads and directly processed for cryo-EM grid
101 preparation. We derived a 3.9 Å resolution cryo-EM 3D map of the OCCM from 304,288
102 particles that were selected from 7500 raw electron micrographs and nearly 1,000,000 raw
103 particles that were recorded on a K2 camera in a Titan Krios microscope operated at a high
104 tension of 300 kV (**Fig. 1a-c, Supplementary Figs. 1-4, Supplementary Table 1,**
105 **Supplementary Video 1, online methods**). The 3D map had well-defined densities for the
106 double strand DNA and 13 subunits of the 14-protein complex (**Fig. 1d and e**). The only protein
107 not well resolved was Orc6; its density was visible only at a lower display threshold.
108 Nevertheless, a conserved C-terminal α -helix of Orc6 was resolved, which is important, as it is
109 mutated in Meier Gorlin syndrome^{37,38}. To better understand the architecture of the complex,
110 and particularly of the flexible sections involving Orc6, cross-linking/mass spectrometry
111 (CLMS) analysis of the OCCM was performed (**Supplementary Fig. 5**), which confirmed the
112 general architecture and also identified several interactions between Orc6 and Orc2/Mcm2 (**Fig.**
113 **2a-c, Supplementary Fig. 6, Supplementary Table 2**). An atomic model of the OCCM was
114 built into the EM densities guided by the published structures of the Mcm2-7 hexamer¹⁴, the
115 *Drosophila* ORC⁷, an archaeal Cdc6 homolog³⁹, a homolog of the N-terminal domain (NTD) of
116 Cdt1, the middle helical domain (MHD) and the C-terminal domain (CTD) of the human Cdt1⁴⁰⁻
117 ⁴². The double stranded DNA was manually built into the EM density (**Supplementary Fig. 7**).
118 Electron densities for eight nucleotides were observed at the interface between Mcm2-Mcm6,
119 Mcm6-Mcm4, Mcm4-Mcm7, Mcm7-Mcm3, Cdc6-Orc1, Orc1-Orc4, Orc4-Orc5, and Orc5-Orc3
120 (**Supplementary Fig. 8**). The nucleotide density at the Orc4-Orc5 interface was the weakest
121 among the eight sites. The Orc5-Orc3 interface was the smallest among the five Orc1-5 subunits,
122 such that the complex could be divided into two sub-complexes of Orc1-Orc4-Orc5 and Orc3-
123 Orc2. However, there was contact between Orc5 and Orc3 at the nucleotide-binding region such
124 that the ATP γ S density at the interface was clear. No nucleotide densities were resolved at
125 interfaces between Mcm3-Mcm5 and Mcm5-Mcm2 due to the reduced resolution and increased
126 flexibility, as they were either at or near the DNA loading gate.

127 In the ORC-Cdc6 top tier of the OCCM, Orc1-5 and Cdc6 formed a six-membered ring structure.
128 The five ORC subunits were arranged in the order of Orc1:Orc4:Orc5:Orc3:Orc2, and Cdc6
129 bridged the gap between Orc1 and Orc2, in agreement with a previous lower resolution EM
130 study (**Fig. 3**)⁵. Interestingly, four WH domains of Mcm3, Mcm4, Mcm6, and Mcm7 spiraled
131 upwards from the Mcm2-7 hexamer and engaged the ORC-Cdc6 ring, each interacting with

132 ORC-Cdc6 subunits (**Fig. 1d and e, Supplementary Figs. 9 and 10**), while an interaction
133 between the Mcm5 WH domain and Orc2 was seen by CLMS (**Fig. 2c**). In the bottom of the
134 Cdt1-Mcm2-7 tier, the six Mcm subunits formed a ring structure in the order of 2-6-4-7-3-5,
135 consistent with previous studies^{14,15,22,43,44}. At the interface between the Mcm2 AAA+ domain
136 and Mcm5 AAA+ domain, the domain swapped α -helix of Mcm5 bound to the Mcm2 AAA+
137 domain, thereby sealing the DNA-loading gate (**Fig. 1c, Supplementary Fig. 11**). Therefore, the
138 C-tier AAA+ ring of the Mcm2-7 hexamer was topologically closed (**Fig. 1d**). However, the N-
139 tier ring was still open at the Mcm2-5 interface. Hence the Mcm2-7 was in a half-open and half-
140 closed state. This structural feature explains why the Mcm2-7 ring in the OCCM is partially salt
141 stable on DNA, but not as salt stable as the Mcm2-7 double-hexamer^{15,31,44}. The structure also
142 explains why the DNA is intact in the C-tier AAA+ ring but invisible in the N-tier ring as DNA
143 in this region may be less constrained or digested by the nuclease, which was used to release the
144 DNA bound OCCM during sample preparation.

145 **ORC-Cdc6 forms a closed ring with a pseudo 6-fold symmetry**

146 In the OCCM structure, ORC-Cdc6 assembled into a complete ring encircling DNA with a
147 pseudo six-fold symmetry (**Fig. 3a-b, Fig. 4**). The N-terminal extension on Orc2 and an insertion
148 in Orc3 give ORC a helical shape⁴⁴. The four observed ATP γ S molecules of ORC-Cdc6 define
149 one circle on top and the four observed nucleotides in Mcm2-7 define another circle below. The
150 top circle is larger, off center, and is tilted by 17° with respect to the lower circle (**Fig. 4a-b**).
151 The six predicted AAA+ proteins, Orc1-5 and Cdc6, all had one AAA+ domain with an AAA-
152 RecA-fold (the RecA fold), an alpha helical-lid domain (the lid), and a C-terminal (CT), alpha
153 helical winged helix domain (WHD), and they were superimposable (**Fig. 3c**)^{45,46}. There were
154 variations to this general rule in that Orc2 lacked the alpha helical lid similar to the DmOrc2, and
155 Orc3 had an insertion consisting of a helical domain. Among the six initiator AAA+ subunits,
156 Orc4 was unique as it had one α -helix insertion and one insertion loop in the WHD. The six
157 AAA-RecA-folds and the six WHD formed a two-tiered ring structure that surrounded the DNA
158 within the central channel. In contrast, the six AAA-lid domains that each bridged the AAA-
159 RecA-like domain and the WH domain formed an outer brace that spiraled around the DNA
160 interacting domains. The bottom tier ring of the WH domains was largely responsible for
161 interacting with the Mcm CTD domains below, as suggested⁷. The peripheral brace of the AAA-
162 lids also interacted with the Mcm subunit WH domains.

163 The crystal structure of the *Drosophila* apo-ORC core revealed an auto-inhibited conformation
164 that is not compatible with DNA binding⁷ (**Fig. 3d**). DmORC structure is also incompatible with
165 Cdc6 binding. However, we found that Orc3-4-5 were in a similar configuration in both ScORC
166 and DmORC. By aligning the two ORC structures using the common Orc3-4-5 region as a
167 reference, we found that the RecA-fold of DmOrc1 and the WH domain of DmOrc2 needed to
168 move and flip by ~180° in order to match their respective yeast counterparts (**Fig. 3e, f**). These
169 changes created a gap between Orc1-Orc2 for DNA passage as well as for Cdc6 insertion
170 between Orc1-Orc2 following DNA binding by ORC (**Fig. 3b, d, Supplementary Video 2**).
171 Since the Mcm2-7 hexamer has been loaded onto DNA by ORC-Cdc6, the conformation of
172 ORC-Cdc6 in the OCCM structure is clearly in its active form, allowing DNA binding⁹ and both
173 Cdc6-Orc1 and Orc1-Orc4 ATPase activities that are required for Mcm2-7 double hexamer
174 assembly or subsequent regulated initiation of DNA replication once per cell division cycle
175 ^{9,29,30,32,47,48}.

176

177 **Cdt1 forms an extended three-domain structure**

178

179 In our previous low-resolution cryo-EM map of OCCM, an electron density outside of Mcm2
180 and Mcm6 was assigned to Cdt1⁴⁴. The current higher resolution EM map clearly showed that
181 Cdt1 exists in an unusually extended three-domain structure, with density outside Mcm2 and
182 Mcm6 assigned to the NTD and middle helical domain (MHD) of Cdt1 (**Fig. 5a-c**). Surprisingly,
183 the Cdt1 CTD was linked to the MHD by a long loop and was 60 Å away from MHD, located
184 between Mcm6 and Mcm4. The density of Cdt1 NTD was relatively weak, indicating a degree of
185 flexibility. The Cdt1 NTD bound only to the Mcm2 CTD with an interface of ~ 600 Å². In
186 contrast, the Cdt1 MHD bound to both NTD and CTD of Mcm2 as well as NTD of Mcm6 with a
187 larger interface of ~ 1000 Å², which was also seen by CLMS (**Fig. 2a**). The Cdt1 CTD interacted
188 extensively with all of the major domains of Mcm6, the Mcm4 NTD, and the Orc4 WH domain
189 insertion loop. Consistent with this observation, a previous NMR study showed interaction
190 between the Mcm6 WH domain and a short peptide in the CTD of Cdt1⁴⁰. Importantly, the Cdt1
191 CTD formed an arch toward the Mcm6 WH domain, which in turn interacted with the Orc4 WH
192 domain and the Orc5 AAA-lid. The Mcm6 WH domain in the Mcm2-7 hexamer before
193 encountering ORC-Cdc6 is likely located in the middle of the ring between Mcm2 and Mcm6,
194 because this is where the domain is found in both active helicase CMG and in the inactive
195 Mcm2-7 double-hexamer (**Fig. 5d**). Hence, the CT arch of Cdt1 is likely responsible for
196 displacing the Mcm6 WHD domain by 40 Å to the periphery where the Mcm6 WHD is found in
197 the OCCM structure. This conformational change likely explains the inhibitory role of the Mcm6
198 WHD, which blocks OCCM formation in the absence of Cdt1³². Therefore, Cdt1 appeared to
199 play a dual role in Mcm2-7 hexamer loading: it created the ORC-Cdc6-binding surface on the
200 CT surface of Mcm2-7 hexamer by moving outward the obstructing Mcm6 WHD, and at the
201 same time formed an extended 3-domain side-brace that stabilized the Mcm2-Mcm6-Mcm4 half
202 ring, potentially allowing the other half ring Mcm5-Mcm3-Mcm7 to move (**Fig. 1d, e**). We
203 suggest that these interactions underlie the essential roles of Cdt1 in Mcm2-7 loading on DNA¹³.
204 Cdt1 bound in the OCCM, particularly its interaction with Mcm2 and the Mcm2-7 subunits that
205 bind ATP (Mcm2,4,7 and 3) may keep the Mcm2-Mcm5 N-tier interface open and prevent
206 Mcm2-7 ATP hydrolysis. ORC-Cdc6 ATPase activity, the next step after OCCM assembly,
207 removes Cdt1³⁰ and may promote Mcm2-7 ATPase activity to close the first Mcm2-7 hexamer
208^{33,34}.

209 To further investigate the interactions between Cdt1 and Mcm2-7, we expressed in baculoviruses
210 each Mcm subunit and Cdt1 as a Strep-Strep-SUMO-Cdt1 (SSS-Cdt1). Each Mcm subunit alone
211 or all six in combination were expressed and a pull down with purified SSS-Cdt1 was performed
212 (**Supplementary Fig. 12**). Cdt1 interacted with all six Mcm proteins when they are expressed
213 together. Individually, Mcm2, Mcm6 (most strongly) but also Mcm7 interact with Cdt1. The
214 former two interactions were found in the OCCM model. We did not see an interaction with
215 Mcm4, suggesting that the Cdt1-CTD interaction with Mcm4 seen in OCCM structure must
216 depend on the prior binding to Mcm2-Mcm6 in the Mcm2-7 hexamer. The interaction with
217 Mcm7 is not present at the stage of OCCM, but could be functional downstream, when OCM
218 recruits the second Cdt1-bound Mcm2-7 hexamer to form the D-H³⁵. A long Mcm7 alpha helix
219 projects down toward the incoming second Mcm2-7-Cdt1 complex (**Fig. 1e**)

220 The Mcm2-7 hexamer in the OCCM needs to change to adopt the structure present in the Mcm2-
221 7 D-H once the loading process is complete. By comparing the two structures, we found that the
222 Mcm2-7 hexamer needed to undergo large conformational changes during the OCCM – D-H
223 transition, in particular within the entire Mcm2-7 NTD ring as well as the CTDs of Mcm2 and
224 Mcm5 (**Fig. 6, Supplementary Video 3**). Specifically, the Mcm2-7 NTD ring needed to rotate
225 by $\sim 25^\circ$ relative to the Mcm2-7 CTD to match the MCM ring in the D-H, and the CTDs of
226 Mcm2 and Mcm5 had to rotate by $\sim 5^\circ$ and $\sim 15^\circ$, respectively, to form the closed interface in the
227 D-H (**Fig. 6b,c**). Because the ATPase activity of Orc1 and Cdc6 is required during the loading
228 reaction^{29,30,32}, and Orc1 and Cdc6 appear in a conformation poised to hydrolyze ATP, it is
229 possible that the conformational changes outlined here are driven by ORC-Cdc6 ATP hydrolysis.
230 Conceivably, the large conformational changes, which could be mediated by interactions
231 between Orc4, Mcm6 and Cdt1 (**Fig. 5a**), would alter the Cdt1 binding surface, leading to its
232 release from Mcm2-7. Since Cdt1 release is known to occur immediately before the recruitment
233 of the second Cdt1-bound Mcm2-7^{30,32,35}, we suggest that ATP hydrolysis by ORC-Cdc6 could
234 facilitate Cdt1 release, completely closing the first Mcm2-7 hexamer and establishing a condition
235 for recruitment of the next Cdt1-bound Mcm2-7 hexamer. Alternatively, MCM ATP-hydrolysis
236 could be involved^{33,34}; however the Mcm2-7 ring is broken in the OCCM, thus ATPase activity
237 of Mcm is likely blocked at this stage⁴⁵.

238 **Asymmetric interaction between ORC-Cdc6 and Cdt1-Mcm2-7 enables DNA insertion**

239 Although both the Mcm2-7 hexamer and ORC-Cdc6 form ring-like structures with a pseudo 6-
240 fold symmetry, the interaction between the two rings is asymmetric due to the $\sim 17^\circ$ tilt of the
241 ORC-Cdc6 ring with respect to the Mcm2-7 ring (**Fig. 1d, Fig. 4**). As a consequence, the DNA is
242 bent by $\sim 20\text{-}25^\circ$ at the interface between ORC-Cdc6 and Mcm2-7. Furthermore, the tilt led to a
243 tight interface between Orc1-Orc4-Orc5 in the first half of the ORC-Cdc6 ring with the Mcm4-
244 Mcm6-Mcm2 half ring, and an apparent “loose” interface between Orc3-Orc2-Cdc6 and Mcm5-
245 3-7. At the tight interface, the WH domains of Orc1 and Orc4 insert into the gaps between the
246 CT WH domains and the AAA-lid domains of Mcm4 and Mcm6; the Orc5 WH domain
247 interacted only with Mcm2 AAA-RecA-fold because Mcm2 lacked a WH domain (**Fig. 1d-e,**
248 **Supplementary Figs. 9-10**). At the “loose interface”, the WH domain of Mcm5 was not visible
249 in the EM map, but the CLMS data identified it across-the-interface partner of Orc2.
250 Interestingly, the WH domains of Mcm3 and Mcm7 reached upwards more than 30 Å via their
251 long loops to interact with Orc2 and Cdc6, respectively (**Fig. 1e, Supplementary Figs. 9, 10**).
252 The loop connecting the AAA-RecA-fold and the WH domain in Mcm7 was ordered and well
253 resolved with slightly weaker density. However, the corresponding loop in Mcm3 was
254 disordered. Accordingly, we propose that the asymmetric interaction leaves half of the Mcm2-7
255 ring (Mcm5-3-7) only loosely tethered, such that the Mcm5-3-7 half ring can move away from
256 the tightly-tethered Mcm4-6-2 half ring to open up the Mcm2/Mcm5 gate for DNA insertion and
257 then move back to close the gate. This conformation is most likely stabilized by Cdt1.

258 259 **Protein-DNA interactions in the OCCM**

260 We modeled 39 base pairs (bp) of DNA in the OCCM density map; 24 bp were encircled by the
261 ORC-Cdc6 ring and the remaining 15 bp by the C-tier ring of Mcm2-7 (**Fig. 7a, Supplementary**
262 **Fig. 13**). There was no apparent DNA density inside the N-tier ring of Mcm2-7. Because the N-

263 tier ring was open at the Mcm2-Mcm5 interface, the dsDNA there might have been digested by
264 the DNase I nuclease that was used to cleave the loading intermediate off of the plasmid DNA.
265 In the top ORC-Cdc6 region, Orc1, Orc3 and Orc5 had little direct interaction with DNA. DNA
266 was held in place by interactions with the initiator-specific motif (ISM) in the AAA+ domains of
267 Orc2, a unique Orc4-specific insertion α -helix, and by the ISM and the WH domains of Cdc6
268 (**Fig. 7a-e**). These four binding components spiraled around the DNA just like RFC clamp
269 loaders spiral around the DNA^{44,49,50}, although the overall ORC-Cdc6 ring itself appears flat
270 because the Orc2 and Orc3 subunits break the helical path. Archaeal AAA+ replication initiators
271 also interact with DNA via their respective ISM^{39,51}. The archaeal WH domain is known to bind
272 DNA with both the helix-turn-helix (HTH) motif and the β -hairpin wing loop⁵¹. However, in the
273 yeast ORC-Cdc6, we found that only the β -hairpin wing loops of the WH domains of Cdc6 and
274 Orc4 bound to DNA, their respective HTH motif did not bind to DNA but rather were engaged
275 in subunit-subunit interactions. This different DNA binding mode was caused by a $\sim 90^\circ$ rotation
276 of the Orc4 and Cdc6 WH domains away from the central DNA channel (**Supplementary Fig.**
277 **14**). We have previously demonstrated that ORC-Cdc6 causes a nuclease protected footprint on
278 the origin DNA that extends to 70-78 base pairs, greater than the 44-50 base-pair footprint of
279 ORC alone⁹. Even allowing for limited nuclease access to the DNA near edges of the ORC-
280 Cdc6 complex, which accounts to 10 bp⁵², the amount of DNA found interacting with ORC-
281 Cdc6 by nuclease footprinting is more than twice that found interacting with ORC-Cdc6 in the
282 OCCM structure. There are positively charged patches in the front side (Orc2,3,6) and the
283 bottom surface of ORC-Cdc6 that is proximal to Mcm2-7 (**Supplementary Fig. 15**). It is
284 possible that DNA bends and binds to some of these surfaces in addition to the central channel.

285 In the lower Cdt1-Mcm2-7 region, Mcm3 and Mcm5 did not interact with DNA. Although the
286 Mcm2-7 ring was nearly flat, the hairpin loops in the AAA+ domains of Mcm2-Mcm4-Mcm6-
287 Mcm7 were arranged in a spiral to grip onto the DNA (**Fig. 7a, f**). We found that Mcm2, Mcm4
288 and Mcm6 interacted with DNA via their respective helix-2-insert (H2I) β -hairpin loop. Mcm4,
289 Mcm6 and Mcm7 contacted the DNA with their respective Presensor 1 (PS1) β -hairpin loops, in
290 particular the well-conserved KA motifs (**Fig. 7f, Supplementary Figs. 13 and 16**). In contrast,
291 the same H2I and PS1 within the Mcm2-7 D-H are involved in inter-subunit interactions¹⁴. In
292 the apo form of the active CMG helicase the PS1 loops face the central DNA channel⁵³, and in a
293 recent cryo-EM structure of CMG at a sub-nanometer resolution, the PS1 loops were found to
294 interact with a 6-base ssDNA⁵⁴. Interestingly, most of these hairpin loops, except for the Mcm4
295 H2I loop, interacted with the same strand of the duplex DNA (**Fig. 7f**). It is unclear if this strand
296 functions as the leading or the lagging strand in the CMG helicase, because extensive
297 conformation changes must occur in Mcm2-7 to form the active helicase, such that Mcm-DNA
298 interaction in the CMG may be very different.

299 **DISCUSSION**

300
301 Since the discovery of ORC more than two decades ago², it has been a key issue in the DNA
302 replication field to identify how ORC recognizes the dsDNA and how ORC cooperates with
303 Cdc6 to load the Mcm2-7 hexamers onto DNA. The current atomic model of the OCCM
304 provides the first high-resolution structure of ORC-Cdc6 bound to origin DNA. Overall, the
305 ORC-Cdc6 structure is flat, but within this structure the subunits that bind ATP, Orc1, Orc4,
306 Orc5 and Cdc6, form a right-handed spiral around the double stranded DNA, similar to the spiral

307 of AAA+ subunits around primer-template DNA in RFC clamp loaders^{49,50}. The human ORC
308 has an almost identical structure (A. Tocilj, K. On, C. Yuan, J. Sun, E. Elkayam, H. Li, B.
309 Stillman and L. Joshua-Tor, submitted). Orc4 had an unusual insertion α -helix that appears to
310 contact the major groove of the dsDNA. This helix is unique to budding yeast Orc4 subunits,
311 being absent in the DmORC and HsORC4 structures⁷ (A. Tocilj, K. On, C. Yuan, J. Sun, E.
312 Elkayam, H. Li, B. Stillman and L. Joshua-Tor, submitted), may help to explain the sequence
313 specificity of ORC that is characteristic of origin binding in *Saccharomyces sp.* Cdc6 is
314 particularly important for DNA binding with two principal DNA binding sites: the ISM and the
315 WH domain, explaining why Cdc6 enhances ORC's specificity for DNA^{9,10}.

316
317 The most prominent feature of Mcm2-7 loading by ORC-Cdc6 is the extensive use of WH
318 domains of these replication proteins. There were six resolved WH domains in ORC-Cdc6 that
319 formed a larger WH ring in the upper tier of the OCCM, and 5 cryo-EM and CLMS resolved
320 WH domains in Mcm2-7 that formed a second slightly smaller WH ring on the lower Mcm2-7
321 tier of the OCCM. This appears to be an evolutionary conserved interaction, as it was reported
322 recently for archaeal MCM and Orc1⁵⁵. However, here we observed that the WHD mediated
323 correct stacking of the two rings mediates much of the recruitment mechanism. The position of
324 the WHD of the Mcm proteins varies widely, and can sit either right above the AAA+ domain, or
325 move away from the main body of the protein, or even move to the side of the AAA+ domain in
326 the case of Mcm5, as seen in the active helicase (**Supplementary Fig. 9b**). The CTD of Cdt1
327 plays a special role in displacing the Mcm6 WH domain to create the ORC-Cdc6 binding
328 surface; we showed previously that the WH domain of Mcm6 is inhibitory and blocks OCCM
329 formation in the absence of Cdt1³². The attachment of the winged helix domains by flexible
330 linker provide these domains manifold possibility to interact with ORC-Cdc6, but after helicase
331 activation, they could also be important interaction partners with other proteins at the DNA
332 replication fork.

333
334 The Mcm2-7 double-hexamer structure, although obtained in the absence of DNA, showed that
335 six H2I hairpin loops are arranged in an approximately helical trajectory that was suggested to
336 facilitate DNA translocation and unwinding. However, in the OCCM, only three H2I hairpin
337 loops of Mcm2-Mcm4-Mcm6 contact DNA. In addition, the three PS1 hairpin loops of Mcm4,
338 Mcm6 and Mcm7 make contact with DNA. In the D-H, the PS1 loop is involved in inter-subunit
339 interaction, not in DNA binding, but in the CMG helicase, the PS1 loop contacts DNA^{14,54}.
340 Another interesting feature of OCCM is the partially open Mcm2-Mcm5 interface. Thus the data
341 provide the first structural proof that the Mcm2-Mcm5 interface is the DNA entry gate in Mcm2-
342 7 during pre-RC formation^{22,31,43}. ATP γ S prevents Cdt1 removal and the gate from closing^{30,32}
343 and thus it is interesting that the N-tier ring is not yet closed given the dsDNA has been loaded
344 into the Mcm2-7 hexamer channel. We suggest that the Mcm2-7 N-tier ring closure requires
345 ATP hydrolysis by Orc1/Cdc6 proteins and removal of Cdt1 from the Mcm2-7 hexamer. The
346 unusually extended three-domain structure of Cdt1 most likely keeps Mcm2-7 subunits vertically
347 aligned, preventing the left-handed spiral of the Mcm2-7 subunits in the completely assembled
348 Mcm2-7 double hexamer (**Fig. 6c**). Thus, like the RFC-PCNA clamp loader and clamp
349 structures, the OCCM structure provides further insight into how a AAA+ complex loads a ring-
350 shaped, multi-subunit complex of proteins around double stranded DNA to promote DNA
351 replication. We suggest that ORC-Cdc6 ATPase promotes complete Mcm2-7 ring closure just as

352 ATP hydrolysis by the clamp loader RFC locks the PCNA DNA polymerase clamp onto double
353 stranded DNA⁵⁰.

354

355 **METHODS**

356 Methods and any associated references are available in the ONLINE METHODS SECTION.

357

358 **Accession Codes** The 3D cryo-EM map of OCCM at 3.9 Å resolution has been deposited at the
359 EMDB database with accession code EMD-xxxx. The corresponding atomic model was
360 deposited at RCSB PDB bank with accession code yyyy.

361

362 **Acknowledgements** Cryo-EM data was collected on a FEI Titan Krios at HHMI Janelia Farm.
363 We also collected a cryo-EM dataset on an FEI Technai F20 equipped with a K2 detector at
364 NRAMM in the Scripps Research Institute, which was supported by NIH grants P41 GM103310.
365 We thank Zhiheng Yu, Chuan Hong, Rick Huang at HHMI, and Clint Porter and Bridget
366 Carragher at Scripps for help with data collection. This work was funded by the US National
367 Institutes of Health (GM111472 and OD12272 to H.L. and GM45436 to B.S.), the
368 Biotechnology and Biological Sciences Research Council UK (P56061 to CS) and the Wellcome
369 Trust (Investigator Award P56628 to CS, Senior Research Fellowship 103139 to JR, a Centre
370 core grant 092076 to JR and an instrument grant 108504 to JR).

371

372 **Author Contributions** Y.Z., A.R., L.B., J.S., J.R., Z.A.C., B.S., C.S. and H.L. designed
373 experiments. Z.Y., A.R., L.B., C.S.P.A., M.B. and J.S. performed experiments. Z.Y., A.R., L.B.,
374 J.S., Z.A.C., J.R., B.S., C.S. and H.L. analyzed the data. L.B., B.S., C.S. and H.L. wrote the
375 manuscript.

376

377 **REFERENCES**

378

- 379 1. Bell, S.P. & Dutta, A. DNA replication in eukaryotic cells. *Annu Rev Biochem* **71**, 333-74
380 (2002).
- 381 2. Bell, S.P. & Stillman, B. ATP-dependent recognition of eukaryotic origins of DNA
382 replication by a multiprotein complex. *Nature* **357**, 128-34 (1992).
- 383 3. Stillman, B. Origin recognition and the chromosome cycle. *FEBS Lett* **579**, 877-84
384 (2005).
- 385 4. Li, H. & Stillman, B. The origin recognition complex: a biochemical and structural view.
386 *Subcell Biochem* **62**, 37-58 (2012).
- 387 5. Chen, Z. et al. The architecture of the DNA replication origin recognition complex in
388 *Saccharomyces cerevisiae*. *Proc Natl Acad Sci U S A* **105**, 10326-31 (2008).
- 389 6. Sun, J. et al. Cdc6-induced conformational changes in ORC bound to origin DNA
390 revealed by cryo-electron microscopy. *Structure* **20**, 534-44 (2012).
- 391 7. Bleichert, F., Botchan, M.R. & Berger, J.M. Crystal structure of the eukaryotic origin
392 recognition complex. *Nature* **519**, 321-6 (2015).
- 393 8. Bell, S.P. & Labib, K. Chromosome Duplication in *Saccharomyces cerevisiae*. *Genetics*
394 **203**, 1027-67 (2016).
- 395 9. Speck, C., Chen, Z., Li, H. & Stillman, B. ATPase-dependent cooperative binding of
396 ORC and Cdc6 to origin DNA. *Nat Struct Mol Biol* **12**, 965-71 (2005).

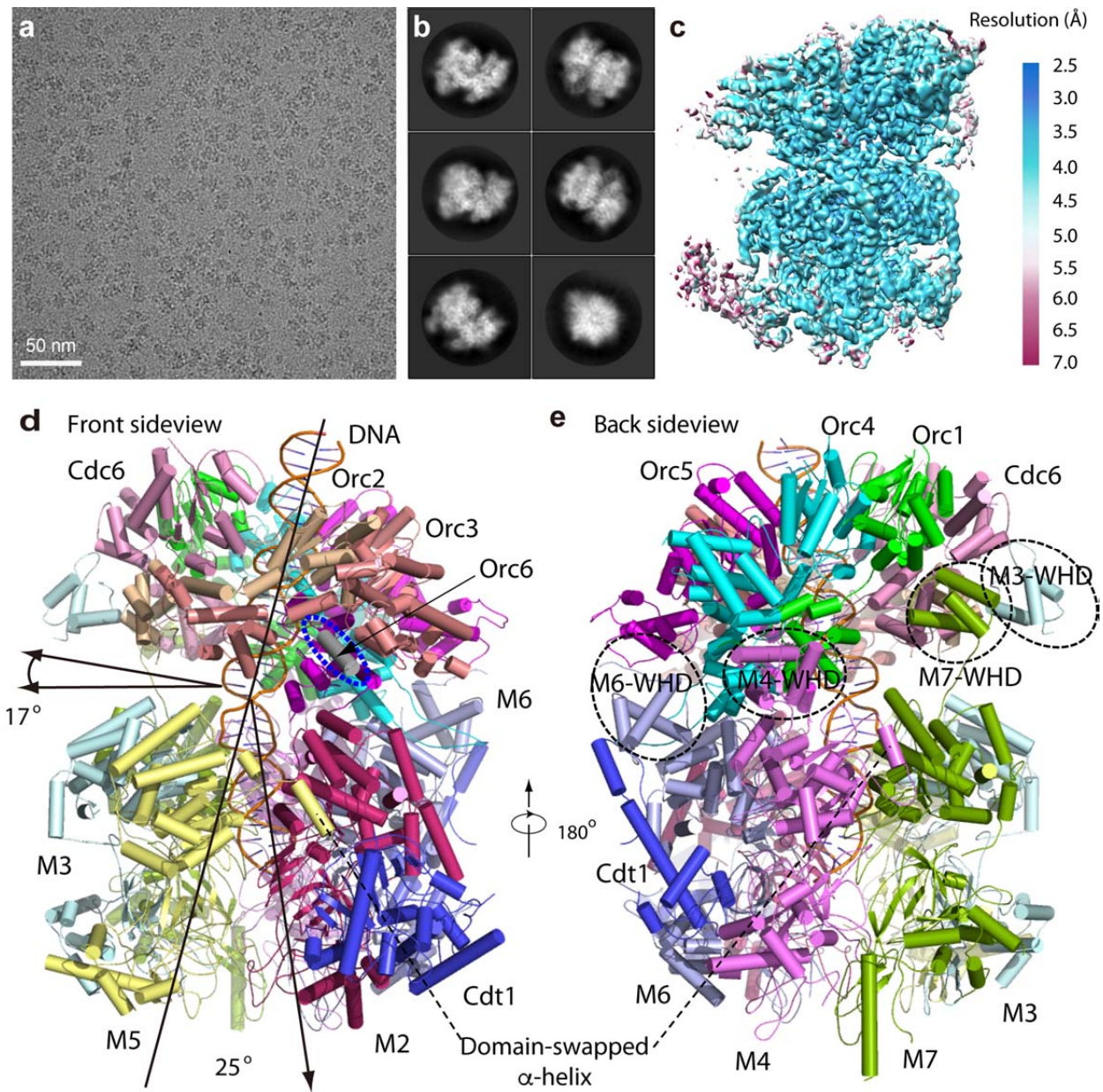
- 397 10. Speck, C. & Stillman, B. Cdc6 ATPase activity regulates ORC x Cdc6 stability and the
398 selection of specific DNA sequences as origins of DNA replication. *J Biol Chem* **282**,
399 11705-14 (2007).
- 400 11. Cocker, J.H., Piatti, S., Santocanale, C., Nasmyth, K. & Diffley, J.F. An essential role for
401 the Cdc6 protein in forming the pre-replicative complexes of budding yeast. *Nature* **379**,
402 180-2 (1996).
- 403 12. Evrin, C. et al. A double-hexameric MCM2-7 complex is loaded onto origin DNA during
404 licensing of eukaryotic DNA replication. *Proc Natl Acad Sci U S A* **106**, 20240-5 (2009).
- 405 13. Remus, D. et al. Concerted loading of Mcm2-7 double hexamers around DNA during
406 DNA replication origin licensing. *Cell* **139**, 719-30 (2009).
- 407 14. Li, N. et al. Structure of the eukaryotic MCM complex at 3.8 Å. *Nature* **524**, 186-91
408 (2015).
- 409 15. Sun, J. et al. Structural and mechanistic insights into Mcm2-7 double-hexamer assembly
410 and function. *Genes Dev* **28**, 2291-303 (2014).
- 411 16. Moyer, S.E., Lewis, P.W. & Botchan, M.R. Isolation of the Cdc45/Mcm2-7/GINS
412 (CMG) complex, a candidate for the eukaryotic DNA replication fork helicase. *Proc Natl*
413 *Acad Sci U S A* **103**, 10236-41 (2006).
- 414 17. Gambus, A. et al. GINS maintains association of Cdc45 with MCM in replisome
415 progression complexes at eukaryotic DNA replication forks. *Nat Cell Biol* **8**, 358-66
416 (2006).
- 417 18. Remus, D. & Diffley, J.F. Eukaryotic DNA replication control: lock and load, then fire.
418 *Curr Opin Cell Biol* **21**, 771-7 (2009).
- 419 19. Yardimci, H., Loveland, A.B., Habuchi, S., van Oijen, A.M. & Walter, J.C. Uncoupling
420 of sister replisomes during eukaryotic DNA replication. *Mol Cell* **40**, 834-40 (2010).
- 421 20. Botchan, M. & Berger, J. DNA replication: making two forks from one prereplication
422 complex. *Molecular Cell* **40**, 860-1 (2010).
- 423 21. Aparicio, T., Guillou, E., Coloma, J., Montoya, G. & Mendez, J. The human GINS
424 complex associates with Cdc45 and MCM and is essential for DNA replication. *Nucleic*
425 *Acids Res* **37**, 2087-95 (2009).
- 426 22. Costa, A. et al. The structural basis for MCM2-7 helicase activation by GINS and Cdc45.
427 *Nat Struct Mol Biol* **18**, 471-7 (2011).
- 428 23. Zegerman, P. & Diffley, J.F. Phosphorylation of Sld2 and Sld3 by cyclin-dependent
429 kinases promotes DNA replication in budding yeast. *Nature* **445**, 281-5 (2007).
- 430 24. Araki, H. Cyclin-dependent kinase-dependent initiation of chromosomal DNA
431 replication. *Curr Opin Cell Biol* **22**, 766-71 (2010).
- 432 25. Sheu, Y.J. & Stillman, B. The Dbf4-Cdc7 kinase promotes S phase by alleviating an
433 inhibitory activity in Mcm4. *Nature* **463**, 113-7 (2010).
- 434 26. Deegan, T.D., Yeeles, J.T. & Diffley, J.F. Phosphopeptide binding by Sld3 links Dbf4-
435 dependent kinase to MCM replicative helicase activation. *EMBO J* **35**, 961-73 (2016).
- 436 27. O'Donnell, M., Langston, L. & Stillman, B. Principles and concepts of DNA replication
437 in bacteria, archaea, and eukarya. *Cold Spring Harb Perspect Biol* **5**(2013).
- 438 28. Yeeles, J.T., Deegan, T.D., Janska, A., Early, A. & Diffley, J.F. Regulated eukaryotic
439 DNA replication origin firing with purified proteins. *Nature* **519**, 431-5 (2015).
- 440 29. Evrin, C. et al. In the absence of ATPase activity, pre-RC formation is blocked prior to
441 MCM2-7 hexamer dimerization. *Nucleic Acids Res* **41**, 3162-72 (2013).

- 442 30. Ticau, S., Friedman, L.J., Ivica, N.A., Gelles, J. & Bell, S.P. Single-molecule studies of
443 origin licensing reveal mechanisms ensuring bidirectional helicase loading. *Cell* **161**,
444 513-25 (2015).
- 445 31. Samel, S.A. et al. A unique DNA entry gate serves for regulated loading of the eukaryotic
446 replicative helicase MCM2-7 onto DNA. *Genes Dev* **28**, 1653-66 (2014).
- 447 32. Fernandez-Cid, A. et al. An ORC/Cdc6/MCM2-7 complex is formed in a multistep
448 reaction to serve as a platform for MCM double-hexamers assembly. *Mol Cell* **50**, 577-88
449 (2013).
- 450 33. Kang, S., Warner, M.D. & Bell, S.P. Multiple functions for MCM2-7 ATPase motifs
451 during replication initiation. *Mol Cell* **55**, 655-65 (2014).
- 452 34. Coster, G., Frigola, J., Beuron, F., Morris, E.P. & Diffley, J.F. Origin licensing requires
453 ATP binding and hydrolysis by the MCM replicative helicase. *Mol Cell* **55**, 666-77
454 (2014).
- 455 35. Evrin, C. et al. The ORC/Cdc6/MCM2-7 complex facilitates MCM2-7 dimerization
456 during prereplicative complex formation. *Nucleic Acids Res* **42**, 2257-69 (2014).
- 457 36. Chang, F. et al. Cdc6 ATPase activity disengages Cdc6 from the pre-replicative complex
458 to promote DNA replication. *Elife* **4**(2015).
- 459 37. Bleichert, F. et al. A Meier-Gorlin syndrome mutation in a conserved C-terminal helix of
460 Orc6 impedes origin recognition complex formation. *Elife* **2**, e00882 (2013).
- 461 38. Balasov, M., Akhmetova, K. & Chesnokov, I. Drosophila model of Meier-Gorlin
462 syndrome based on the mutation in a conserved C-Terminal domain of Orc6. *Am J Med*
463 *Genet A* **167A**, 2533-40 (2015).
- 464 39. Gaudier, M., Schuwirth, B.S., Westcott, S.L. & Wigley, D.B. Structural basis of DNA
465 replication origin recognition by an ORC protein. *Science* **317**, 1213-1216 (2007).
- 466 40. Liu, C. et al. Structural insights into the Cdt1-mediated MCM2-7 chromatin loading.
467 *Nucleic acids research* **40**, 3208-3217 (2012).
- 468 41. Wei, Z. et al. Characterization and structure determination of the Cdt1 binding domain of
469 human minichromosome maintenance (Mcm) 6. *J Biol Chem* **285**, 12469-73 (2010).
- 470 42. Lee, C. et al. Structural basis for inhibition of the replication licensing factor Cdt1 by
471 geminin. *Nature* **430**, 913-917 (2004).
- 472 43. Bochman, M.L. & Schwacha, A. The MCM2-7 complex has in vitro helicase activity. *Mol*
473 *Cell* **31**, 287-93 (2008).
- 474 44. Sun, J. et al. Cryo-EM structure of a helicase loading intermediate containing ORC-
475 Cdc6-Cdt1-MCM2-7 bound to DNA. *Nat Struct Mol Biol* **20**, 944-51 (2013).
- 476 45. Enemark, E.J. & Joshua-Tor, L. On helicases and other motor proteins. *Curr Opin Struct*
477 *Biol* **18**, 243-57 (2008).
- 478 46. Neuwald, A.F., Aravind, L., Spouge, J.L. & Koonin, E.V. AAA+: A class of chaperone-
479 like ATPases associated with the assembly, operation, and disassembly of protein
480 complexes. *Genome Res* **9**, 27-43 (1999).
- 481 47. Bowers, J.L., Randell, J.C., Chen, S. & Bell, S.P. ATP hydrolysis by ORC catalyzes
482 reiterative MCM2-7 assembly at a defined origin of replication. *Mol Cell* **16**, 967-78
483 (2004).
- 484 48. Frigola, J., Remus, D., Mehanna, A. & Diffley, J.F. ATPase-dependent quality control of
485 DNA replication origin licensing. *Nature* **495**, 339-43 (2013).
- 486 49. O'Donnell, M. & Kuriyan, J. Clamp loaders and replication initiation. *Curr Opin Struct*
487 *Biol* **16**, 35-41 (2006).

488 50. Kelch, B.A., Makino, D.L., O'Donnell, M. & Kuriyan, J. How a DNA polymerase clamp
489 loader opens a sliding clamp. *Science* **334**, 1675-80 (2011).
490 51. Dueber, E.L.C., Corn, J.E., Bell, S.D. & Berger, J.M. Replication origin recognition and
491 deformation by a heterodimeric archaeal Orc1 complex. *Science* **317**, 1210-1213 (2007).
492 52. Suck, D. & Oefner, C. Structure of DNase I at 2.0 Å resolution suggests a mechanism for
493 binding to and cutting DNA. *Nature* **321**, 620-5 (1986).
494 53. Yuan, Z. et al. Structure of the eukaryotic replicative CMG helicase suggests a pumpjack
495 motion for translocation. *Nat Struct Mol Biol* **23**, 217-24 (2016).
496 54. Abid Ali, F. et al. Cryo-EM structures of the eukaryotic replicative helicase bound to a
497 translocation substrate. *Nat Commun* **7**, 10708 (2016).
498 55. Samson, R.Y., Abeyrathne, P.D. & Bell, S.D. Mechanism of Archaeal MCM Helicase
499 Recruitment to DNA Replication Origins. *Mol Cell* **61**, 287-96 (2016).

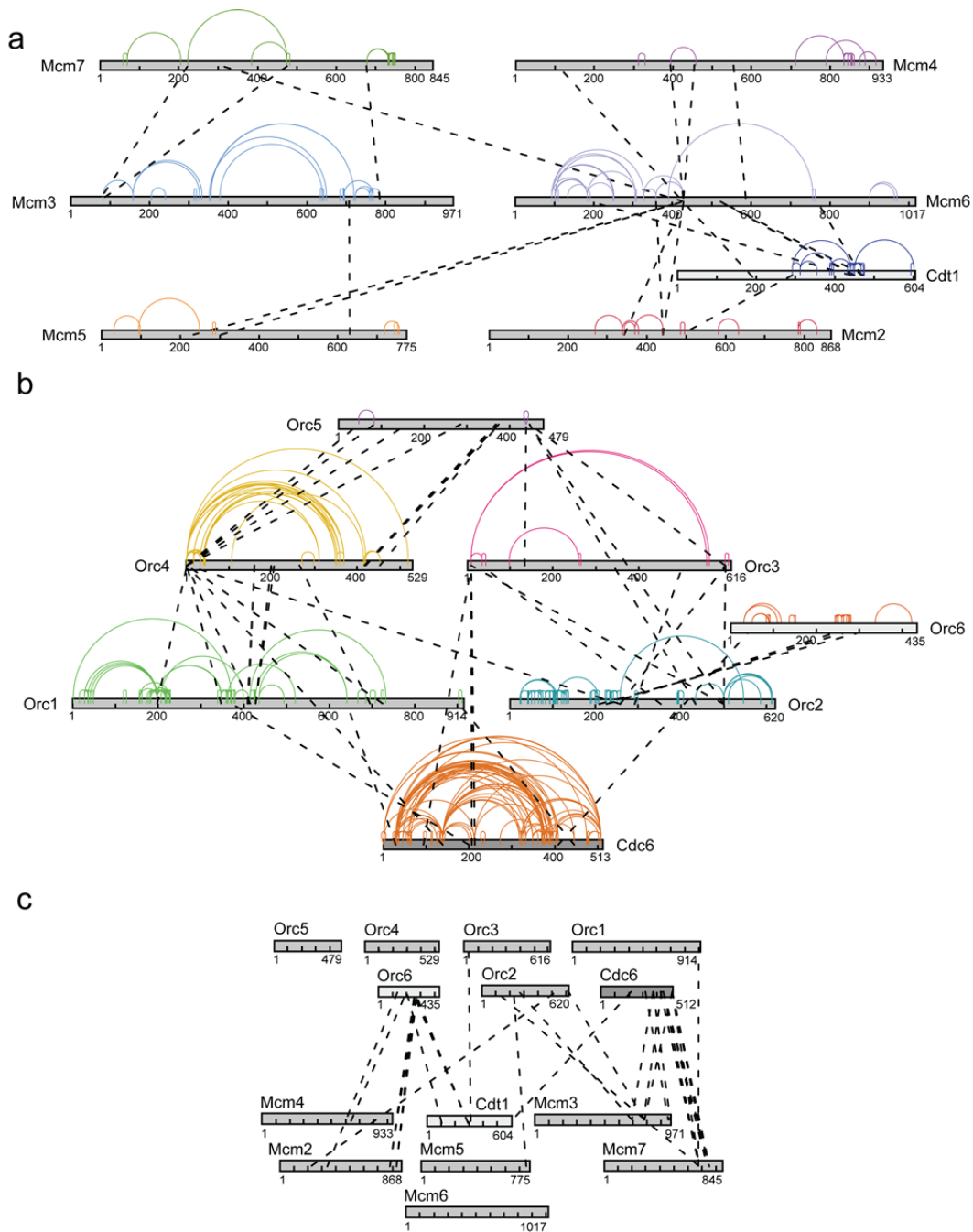
500
501
502
503
504
505
506
507
508
509
510
511
512
513
514
515
516
517
518
519
520
521
522
523
524
525
526
527
528
529
530
531

Figure legends



532
 533
 534
 535
 536
 537
 538
 539
 540
 541
 542
 543

Figure 1. Cryo-EM and overall structure of the *S. cerevisiae* OCCM complex. (a) A typical motion-corrected raw image of frozen OCCM particles recorded on a direct detector. (b) Selected six 2D averages representing the particles in different views. (c) 3D cryo-EM map of OCCM color coded by local resolution. Overall resolution is 3.9 Å. (d) Cartoon view of the atomic model of OCCM as viewed from Front side. The two black arrows in left indicates that the ORC-Cdc6 ring lays on the MCM ring tilted by an angle of ~17°. The two black arrows in middle shows the DNA in central channel is bent by ~25°. The blue oval marks the short helix of Orc6. (e) Cartoon view of the OCCM model as viewed from the backside. The black circles mark the WHDs of Mcm3, Mcm4, Mcm6 and Mcm7, respectively.



544

545 **Figure 2. Cross-linking/mass spectrometry analysis of *S. cerevisiae* OCCM complex. (a)**

546 Linkage map showing the observed cross-linked residue pairs within the MCM2-7/Cdt1

547 complex. Intra-molecular cross-links are color coded, while inter-molecular cross-links are

548 shown in black. (b) Linkage map showing the observed cross-linked residue pairs within the

549 ORC/Cdc6 complex. Intra-molecular cross-links are color coded, while inter-molecular cross-

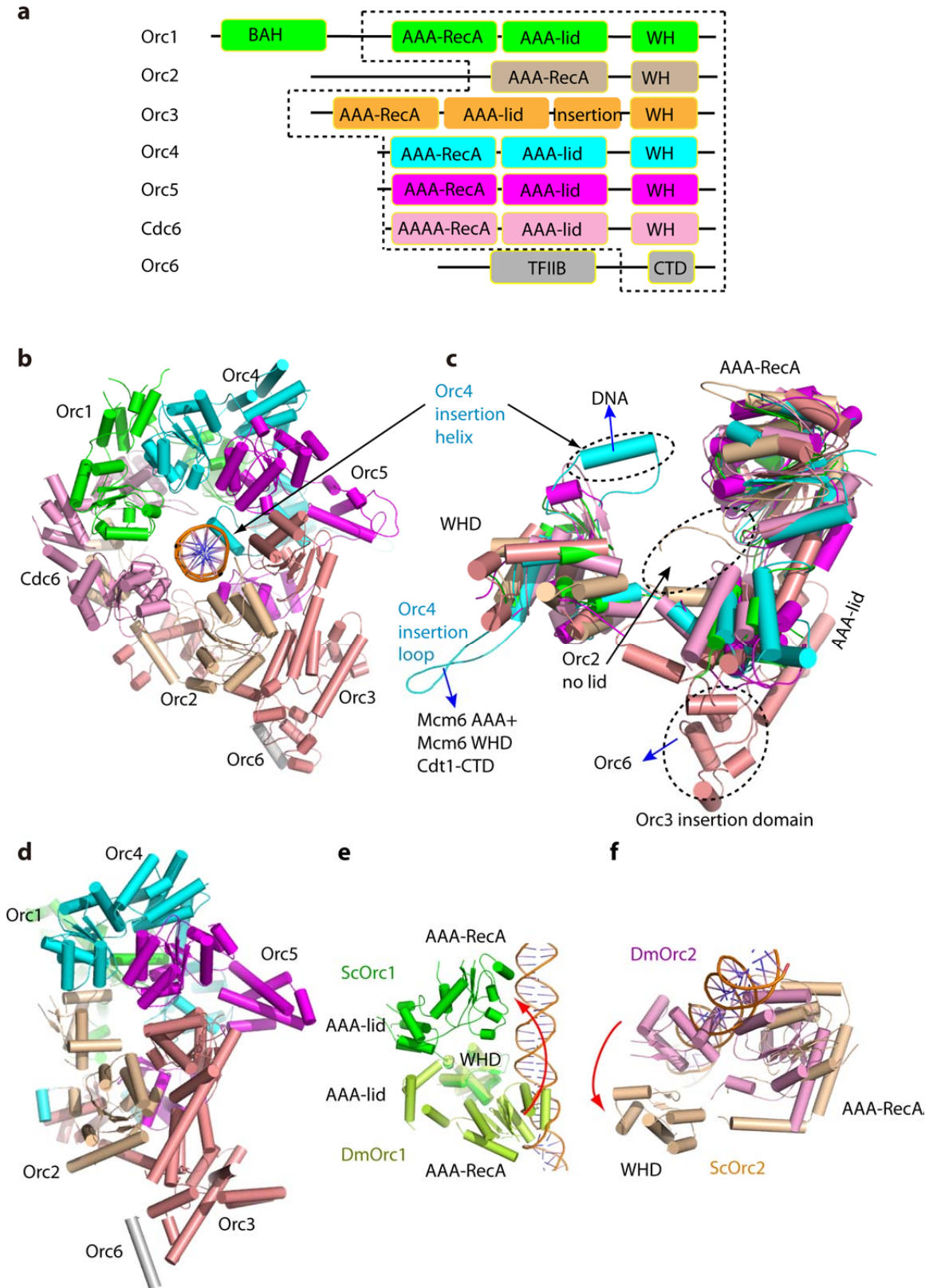
550 links are shown in black. (c) Linkage map showing the observed cross-linked residue pairs

551 between ORC/Cdc6 complex and Mcm2-7/Cdt1 complex. Orc6, which was only partially

552 resolved by cryo-EM, is in close proximity to Mcm2 and Cdt1. The Winged Helix Domain of

553 Mcm5, that was only partially resolved by cryo-EM, is in close proximity to the N-terminal

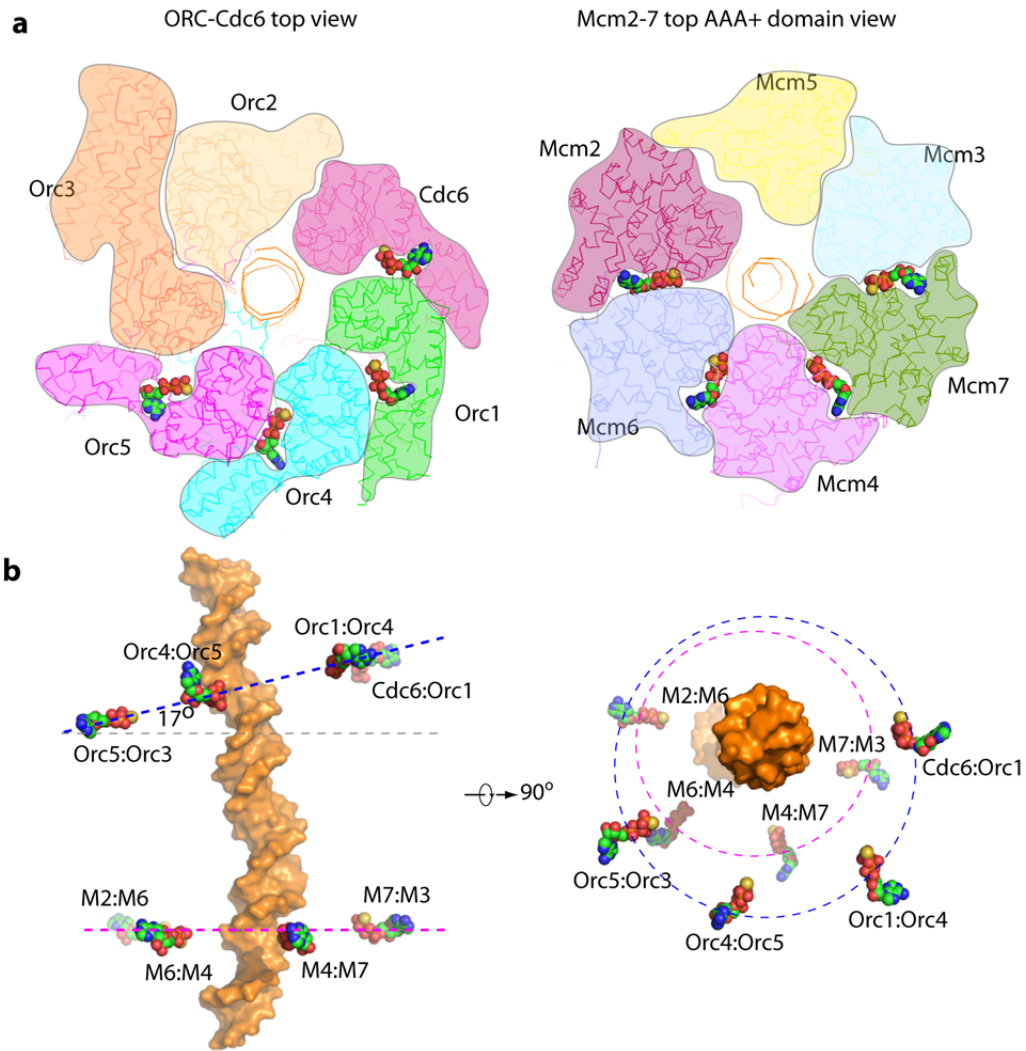
554 region of Orc2.



555
556
557

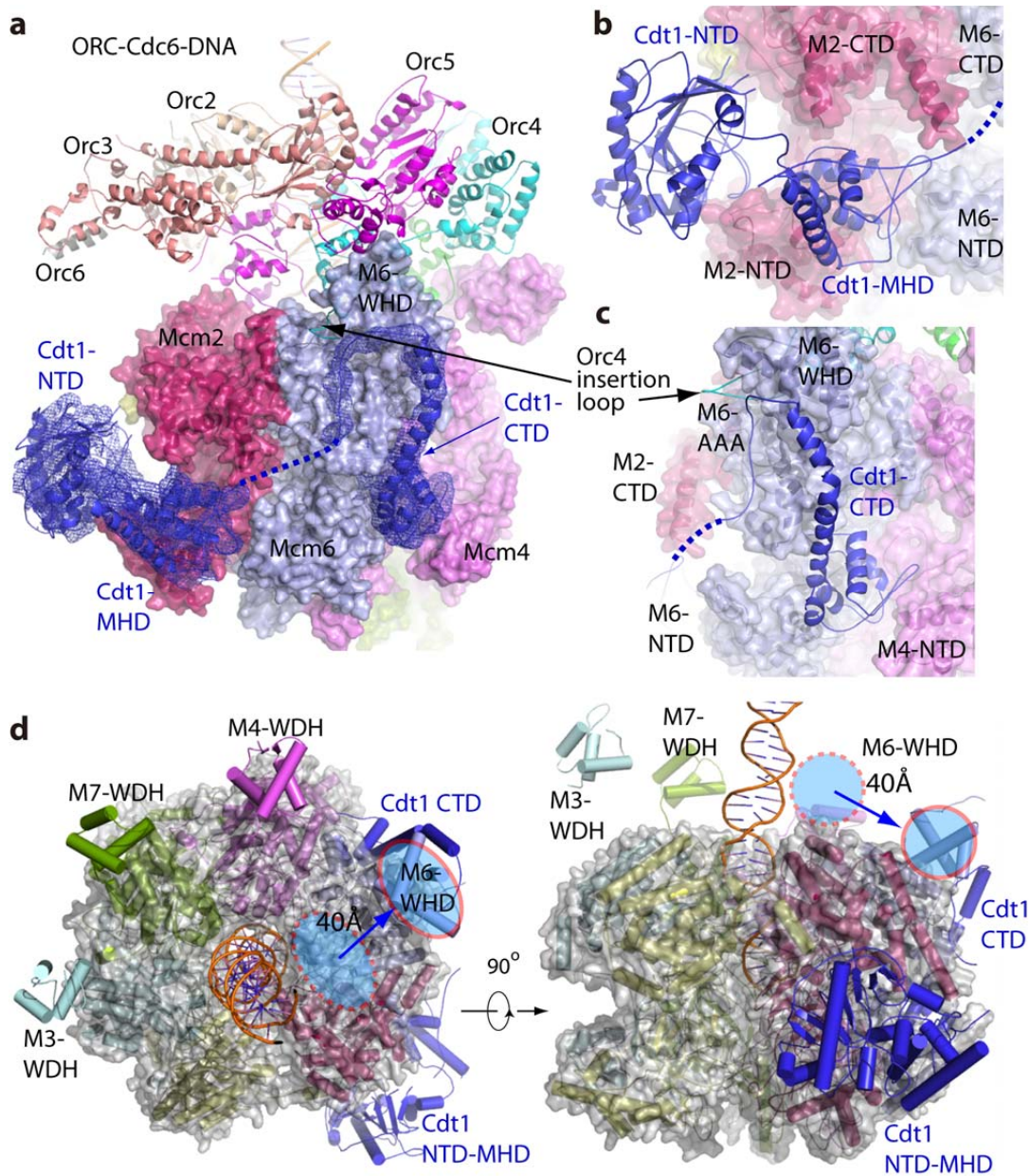
Figure 3. ORC-Cdc6 encircles the origin DNA with the Orc4 insertion helix binding to a major groove. (a) Domain organization of *S. cerevisiae* Orc1-5 subunits and Cdc6. Dashed lines

558 mark the ORC-Cdc6 core regions resolved in our model (TFIIB and CTD, transcription factor-II-
559 like and C-terminal domains in Orc6; BAH, bromo-adjacent homology domain in Orc1). **(b)** The
560 ORC-Cdc6 structure in our *S. cerevisiae* OCCM model in top view. **(c)** Superposition of Orc1-5
561 and Cdc6, highlighting their similar overall structures. Orc2 lacked the AAA-lid domain,
562 resulting in a relatively open interface between Orc2-Cdc6. Orc3 had an insertion domain
563 between the AAA-lid domain and the WHD domain that interacted with Orc6. The blue arrows
564 point to structures with which these marked elements interact. The black arrow points to the
565 missing lid domain in Orc2. **(d)** Crystal structure of *Drosophila* ORC complex in a similar
566 subunit color scheme. **(e, f)** Alignment of DmORC with ScORC-Cdc6 using the most similar
567 Orc3-5 region as a reference showed that the AAA-RecA-fold domain of DmOrc1 **(e)** and WHD
568 of DmOrc2 **(f)** needed to move and rotate by 180° to assume their respective position in
569 ScOCCM. See also Supplemental video 1.
570



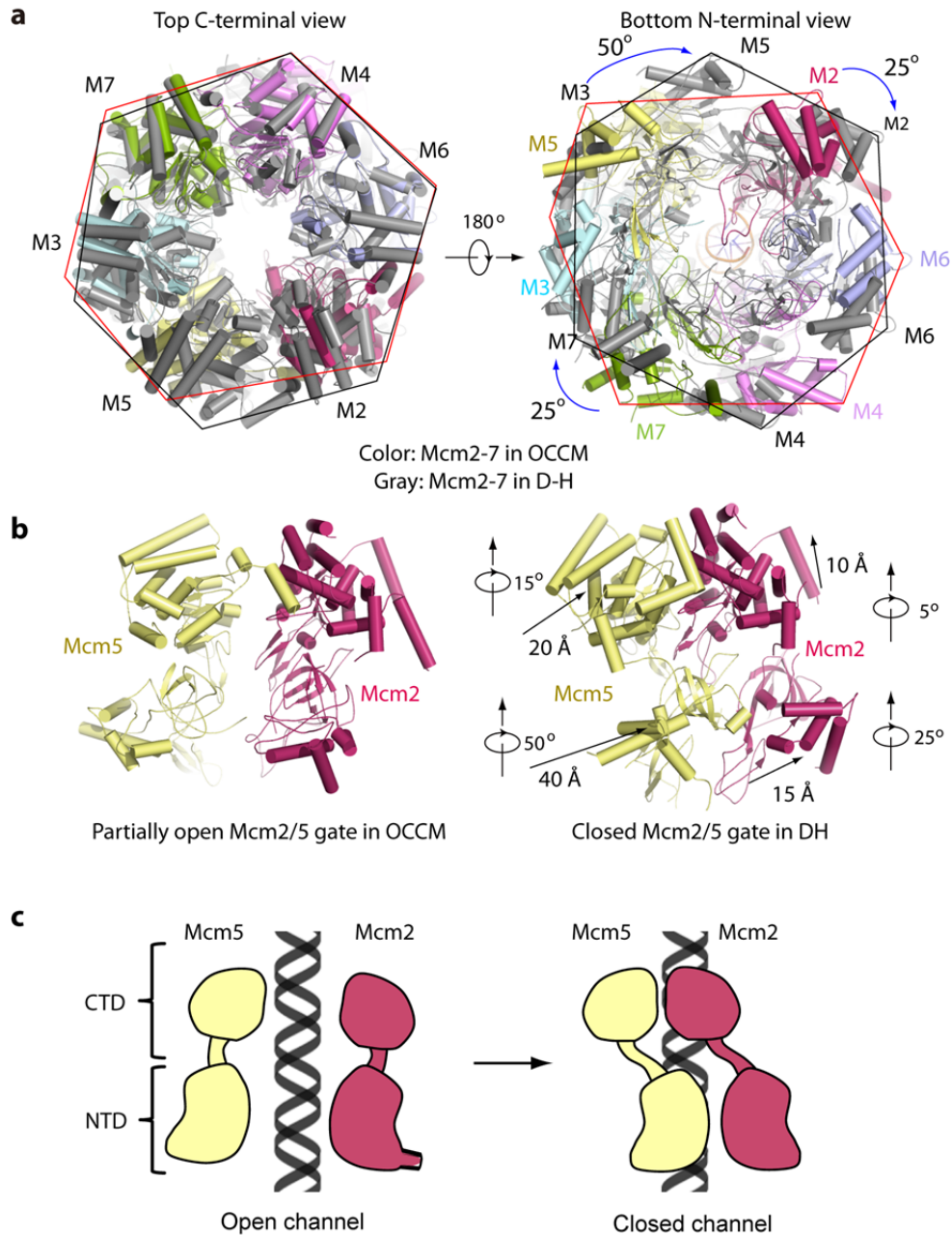
571
 572
 573
 574
 575
 576
 577
 578
 579
 580
 581
 582
 583
 584
 585
 586
 587

Figure 4. Nucleotide binding sites and configuration in OCCM. (a) Cut-open top view of ORC-Cdc6 and Mcm2-7 shown in surface view. The four ATPγS molecules identified in ORC-Cdc6 at the interface between Cdc6-Orc1, Orc1-Orc4, Orc4-Orc5, and Orc5-Orc3 (right), and four ATPγS molecules in Mcm2-7 at the interface between Mcm2-Mcm6, Mcm6-Mcm4, Mcm4-Mcm7, and Mcm7-Mcm3 are shown as spheres (carbon in green, oxygen in red, nitrogen in blue, sulfur in yellow). (b) The positions of the observed nucleotides in OCCM relative to the DNA, which is shown in orange surface. The left panel is a side view with Mcm4 in front and the right panel is a top view with ORC-Cdc6 on top, but proteins are not shown in order to highlight the nucleotides. The four ATPγS molecules in ORC-Cdc6 are co-planar, but the plane is tilted by ~17° with respect to the plane formed by the nucleotides in Mcm2-7. An imaginary circle defined by the nucleotide in ORC-Cdc6 is larger (75 Å) than the circle defined by nucleotides in Mcm2-7 (65 Å), and the two circles are acentric.

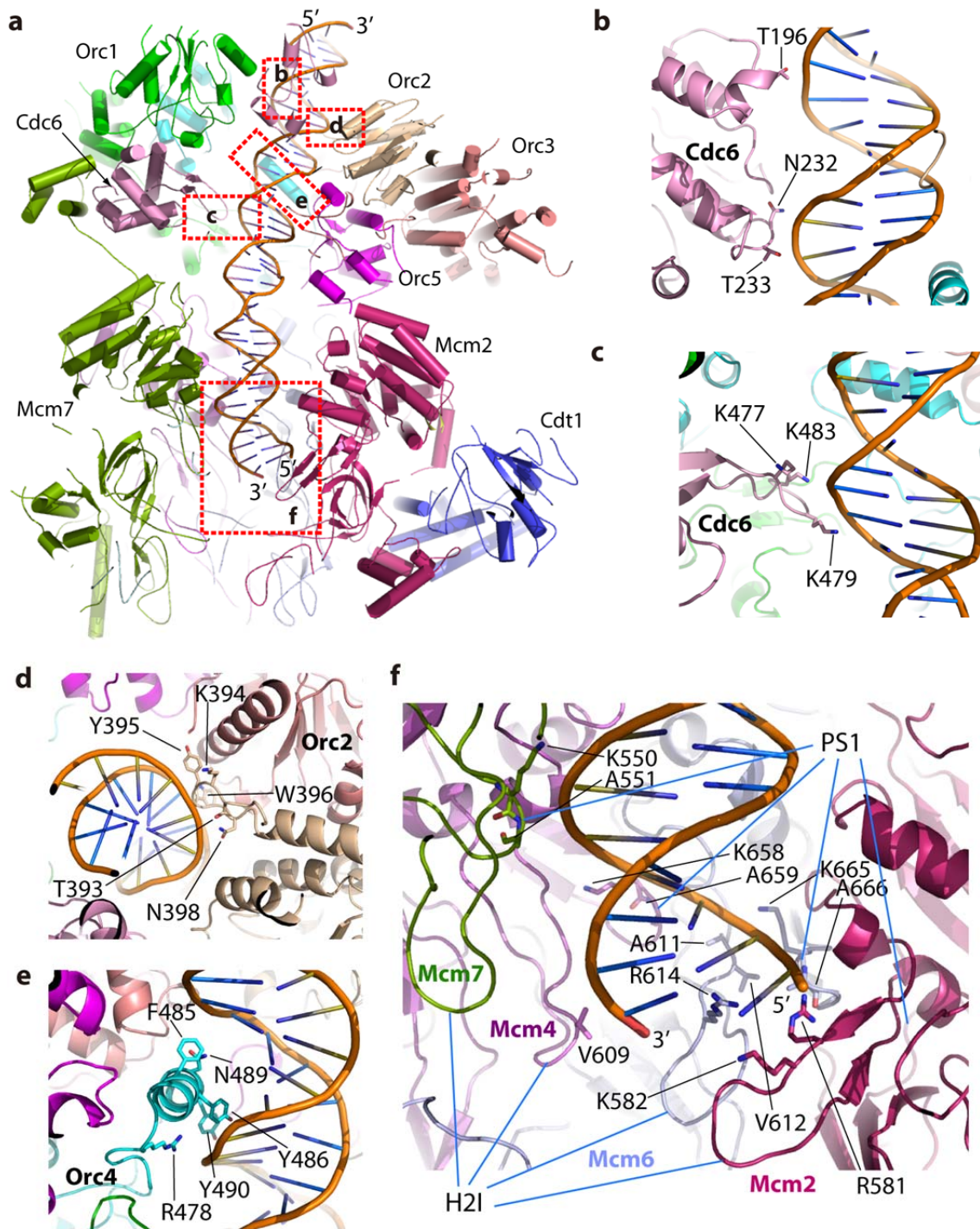


588
589

590 **Figure 5. Extensive interactions between Cdt1 and MCM hexamer.** (a) OCCM structure with
591 Cdt1 electron density shown in blue mesh. The CTD of Cdt1 locates between Mcm6 and Mcm4,
592 over 60 Å away from the NTD and MHD of Cdt1. (b) Zoomed view of the Cdt1 NTD and MHD
593 showing their interactions with Mcm2 and Mcm6. (c) Zoomed view showing the Cdt1 CTD
594 interacting with Mcm6 WHD. The dotted blue line in (a-c) indicates a flexible loop connecting
595 Cdt1 MHD and CTD. (d) The top view (left) and front side view (right) of Mcm2-7 structure in
596 cartoon and semi-transparent surface view. The red oval marks Mcm6-WHD in OCCM, and the
597 dashed red oval the position of Mcm6-WHD in CMG helicase. The blue arrow shows the
598 displacement of Mcm6 WHD in OCCM due to interaction with Cdt1 CTD. Such displacement
599 forms an unobstructed Mcm2-7 C-terminal face for binding with ORC-Cdc6.
600



601
 602 **Figure 6. Conformational changes between the Mcm2-7 in OCCM and double-hexamer (D-**
 603 **H).** (a) Comparison of the top CTD view (left) and the bottom NTD view (right) of the Mcm2-7
 604 structure in the double-hexamer (gray cartoon) with the Mcm2-7 structure in the OCCM. The
 605 two structures were aligned using CTDs of Mcm4-6-7 as reference. Changes in the CTD ring are
 606 focused in Mcm2-5-3. The NTD ring rotated en bloc by about 25°. (b) Front Mcm2/5 side view
 607 of the Mcm2-7 hexamer in the OCCM structure (left) as compared to that in the D-H (right).
 608 Transitioning from OCCM to double hexamer, each CTD AAA+ domain and NTD of Mcm2 and
 609 Mcm5 undergoes a combination of rotation and translation, with the degree of rotation and
 610 translation shown as labeled. Mcm5 NTD needs to rotate by as much as 50° to close the DNA
 611 entry gate. (c) A sketch showing how the gate between Mcm2 and Mcm5 can be open for DNA
 612 insertion in OCCM (left) and how the gate is closed in the D-H (right).



613
 614
 615
 616
 617
 618
 619
 620
 621

Figure 7. Interactions between OCCM and DNA. (a) An overview of OCCM-DNA structure in side view. Subunits in front of DNA including parts of Orc1 and Cdc6, and all of Mcm3 and Mcm5 are removed to show DNA. Five rectangle-marked areas are enlarged in panels (c-f). (b-c) Detailed view of the Cdc6 interaction with dsDNA. (d) Orc2 interaction with DNA. (e) Orc4 interaction with DNA. (f) Mcm2-6-4-7 and DNA interfaces. PS1: Pres-sensor 1 β -hairpin loop, H2I: Helix-2-insert β -hairpin loop.

622 **EXPERIMENTAL PROCEDURES**

623

624 **Sample preparation and electron microscopy**

625 The *Saccharomyces cerevisiae* loading intermediate OCCM was assembled *in vitro* with purified
626 ORC, Cdc6, Cdt1 and Mcm2-7 on plasmid DNA containing the ARS1 sequence in the presence
627 of ATP γ S, and isolated by the magnetic beads pull-down approach as described previously⁴⁴
628 with minor modifications. 24 pre-RC reactions containing 40 nM ORC, 80 nM Cdc6, 40 nM
629 Cdt1, 40 nM MCM2-7 and 6 nM pUC19-ARS1 beads in 50 μ l buffer A (50 mM HEPES-KOH
630 (pH 7.5), 100 mM potassium glutamate, 10 mM magnesium acetate, 50 μ M zinc acetate, 3 mM
631 ATP γ S, 5 mM DTT, 0.1% Triton X-100 and 5% glycerol) were incubated for 15 min at 24 °C.
632 After three washes with buffer B (50 mM HEPES-KOH (pH 7.5), 100 mM K acetate, 3 mM
633 ATP γ S) the complex was eluted with 1 U of DNase I in buffer B and 1 mM CaCl₂.

634 To prepare cryo-EM grids, we pooled all the elutions together and concentrated the sample to
635 about 0.9 mg/ml in buffer B with a Microcon centrifugal filter unit (YM-100 membrane). Before
636 EM grid preparation, we checked the sample for homogeneity by negative-stain electron
637 microscopy. We then applied 3 μ l of OCCM sample at a final concentration of 0.9 mg/ml to
638 glow-discharged C-flat 1.2/1/3 holey carbon grids, incubated for 10 s at 6 °C and 95% humidity,
639 blotted for 3 s then plunged into liquid ethane using an FEI Vitrobot IV. We loaded the grids into
640 an FEI Titan Krios electron microscope operated at 300 kV high tension and collected images
641 semi-automatically with SerialEM under low-dose mode at a magnification of \times 29,000 and a
642 pixel size of 1.01 Å per pixel. A Gatan K2 summit direct electron detector was used under super
643 resolution mode for image recording with an under-focus range from 1.5 to 3.5 μ m. The dose
644 rate was 10 electrons per Å² per second and total exposure time was 5 seconds. The total dose
645 was divided into a 25-frame movie and each frame was exposed for 0.2 s.

646

647 **Image processing and 3D reconstruction**

648 Approximately 7500 raw movie micrographs were collected. The movie frames were first
649 aligned and superimposed by the program Motioncorr⁵⁶. Contrast transfer function parameters
650 of each aligned micrograph were calculated using the program CTFFIND4⁵⁷. All the remaining
651 steps, including particle auto selection, 2D classification, 3D classification, 3D refinement, and
652 density map post-processing were performed using Relion-1.4⁵⁸. We manually picked \sim 10,000
653 particles from different views to generate 2D averages, which were used as templates for
654 subsequent automatic particle selection. Automatic particle selection was then performed for the
655 entire data set. 1,371,667 particles were initially selected. Then we carefully checked the
656 particles obtained from automatically picking, removed the bad particles and re-picked the
657 missing good ones. Particles were then sorted by similarity to the 2D references; the 10% of
658 particles with the lowest z-scores were deleted from the particle pool. 2D classification of all
659 remaining particles was performed and particles in unrecognizable classes by visual inspection
660 were removed. A total of 601,095 particles were used for 3D classification. We derived six 3D
661 models from the dataset, and found two models were similar to each other and their associated
662 particles were combined for further refinement; the other four models were distorted and those
663 particles were discarded, leading to a dataset size of 304,288 particles. This final dataset was
664 used for further 3D refinement, resulting in the 3.91 Å 3D density map. The resolution of the

665 map was estimated by the so-called gold-standard Fourier shell correlation, at the correlation
666 cutoff value of 0.143. The 3D density maps were corrected for the detector modulation transfer
667 function and sharpened by applying a negative B-factor of -112 \AA^2 . The particles had some
668 preference for end-on views but because of the large number of particles used virtually all of the
669 angular space was sampled.

670

671 **Structural modeling, refinement, and validation**

672 The yeast Mcm2-7 models were directly extracted from the cryo-EM structure of the yeast
673 Mcm2-7 double hexamer (PDB code 3JA8)¹⁴. For subsequent docking, each Mcm proteins was
674 split into 2 parts: NTD and CTD. The initial models of the *S. cerevisiae* Orc1-5 subunits were
675 generated from the crystal structure of the *Drosophila* ORC complex (PDB ID: 4XGC)⁷ and
676 Cdc6 subunit from the homologue Archaeal structure (PDB ID: 2V1U)³⁹ using the SWISS-
677 MODEL server⁵⁹. These models were first docked and fitted into the density map using COOT
678⁶⁰ and Chimera⁶¹. We found Orc1 and Orc2 in the yeast OCCM had gone through dramatic
679 conformational changes compared to the fly ORC structure. Thus, we split each of the two
680 proteins into 3 parts: the AAA-RecA-fold and the AAA-lid domain (where present) and the C-
681 terminal WH domain, and fitted these domains independently into the 3D density map. Based on
682 the structural features, the extra density outside Mcm2 and Mcm6 clearly belonged to NTD and
683 middle helical domain (MHD) of Cdt1⁴⁴. We used the SWISS-MODEL server to generate the
684 atomic models of Cdt1 NTD and MHD from their respective homologous structures (PDB ID:
685 5C3P and 2ZXX)^{42,62}. The Cdt1 CTD model was generated from human Cdt1 crystal structure
686 (PDB ID: 2WVR)⁶³, and this domain was found in the region between Mcm6 and Mcm4. Four
687 bulky densities outside the core structure of Cdc6-ORC were identified to be the WH domains of
688 Mcm3, Mcm4, Mcm6, and Mcm7, respectively. Their atomic models were generated from their
689 corresponding homologue structures (PDB ID: 3NW0, 2M45, 2KLQ, and 2OD5)^{41,64,65} using
690 the SWISS-MODEL server. The Orc6 density was very weak, indicating high flexibility of this
691 protein. However, based on the homologous *Drosophila* ORC core complex structure (PDB ID:
692 4XGC)⁷, we identified a short α -helix at the C-terminus of Orc6 that bond to and was stabilized
693 by Orc3. Finally, the double stranded DNA was built into the long helical density that ran
694 through the OCCM structure in the program COOT. The entire OCCM atomic model was
695 subsequently adjusted manually and rebuilt in COOT. Clearly resolved bulky residues such as
696 Phe, Tyr, Trp, and Arg were used for sequence registration.

697

698 The manually built atomic model was then iteratively refined in real space by
699 phenix.real_space_refine⁶⁶ and rebuilt in COOT. We also performed the reciprocal space
700 refinement procedure with the application of secondary structure and stereochemical constraints
701 in the program Phenix⁶⁷. The structure factors (including phases) were calculated by Fourier
702 transform of the experimental density map with the program Phenix.map_to_structure_factors.
703 The atomic model was validated using MolProbity⁶⁸. Structural figures were prepared in
704 Chimera and Pymol (<https://www.pymol.org>).

705

706 The final model was cross validated using a method described previously⁶⁹. Briefly, we
707 randomly added 0.1 \AA noise to the coordinates of the final model using the PDB tools in Phenix,
708 then refined the noise-added against the first half map (Half1) that was produced from one half
709 of the particle dataset during refinement by RELION. We performed one round of coordinate
710 refinement, followed by a B-factor refinement. The refined model was then correlated with the

711 3D maps of the two half maps (Half1, Half2) in Fourier space to produce two FSC curves:
712 FSC_{work} (model versus Half1 map) and FSC_{free} (model versus Half2 map), respectively. A third
713 FSC curve was calculated between the refined model and the final 3.9 Å resolution density map
714 produced from all particles. The general agreement of these curves was taken as an indication
715 that the model was not over-fitted.

716

717 **Cross-linking/Mass Spectrometry analysis**

718 240 nM pUC19-ARS1 beads were used to assemble the OCCM complex as previously
719 described. The complex was cross-linked in the presence of the beads with BS3 1:8100 (molar
720 protein:cross-linker ratio) for 2 hours at 4 °C. Then, the reaction was quenched with 50 ul of
721 saturated ammonium bicarbonate for 45 minutes at 4 °C and it was transferred into digestion
722 buffer (50 mM ammonium bicarbonate, 8 M Urea) followed by reduction with DTT and
723 alkylation with iodoacetamide. 3 ug LysC (with estimated 1:50 enzyme to protein ratio) were
724 added and incubated at room temperature for 4 hours. The digestion buffer was then diluted with
725 50 mM ammonium bicarbonate to a final Urea concentration of 2M. 3 ug of trypsin were added
726 (at estimated 1:50 enzyme to protein ratio) and incubated for 16 hours at room temperature. After
727 digestion, the supernatant was collected and acetified using 200 ul 10% Trifluoroacetic acid
728 (TFA). The peptide mixture was then desalted using C18-Stage-Tips for mass spectrometric
729 analysis⁷⁰. LC-MS/MS analysis was performed using an Orbitrap Fusion™ Lumos™ Tribrid™
730 Mass Spectrometer (Thermo Scientific) applying a “high-high” acquisition strategy⁷¹. 2 ug
731 peptide mixture was injected for each mass spectrometric acquisition. Peptides were separated on
732 a 50 centimeter EASY-Spray column (Thermo Scientific) assembled in an EASY-Spray source
733 (Thermo Scientific), operated at 50 °C column temperature. Mobile phase A consisted of water,
734 0.1% v/v formic acid and 5% v/v DMSO. Mobile phase B consisted of 80% v/v acetonitrile,
735 0.1% v/v formic acid and 5% v/v DMSO. Peptides were loaded at a flow-rate of 0.3 µl/min and
736 eluted at 0.2 µl/min using a linear gradient going from 2% mobile phase B to 40% mobile phase
737 B over 139 minutes, followed by a linear increase from 45% to 95% mobile phase B in 12
738 minutes. The eluted peptides were directly introduced into the mass spectrometer. MS data was
739 acquired in the data-dependent mode with the top-speed option. For each three-second
740 acquisition cycle, the mass spectrum was recorded in the Orbitrap with a resolution of 120,000.
741 The ions with a precursor charge state between 3+ and 8+ were isolated and fragmented. The
742 fragmentation spectra were then recorded in the Orbitrap. Dynamic exclusion was enabled with
743 single repeat count and 60-second exclusion duration. To improve the identification of cross-
744 linked peptides, in total 9 acquisitions were carried out with variations on parameters mainly
745 related to criteria for ion selection for fragmentation and fragmentation methods.

746 **Identification of cross-linked peptides**

747 The raw mass spectrometric data files were processed into peak lists using MaxQuant version
748 1.5.2.8⁷² with default parameters, except for “FTMS top peaks per 100 Da” was set to 20 and
749 “FTMS de-isotoping” was disabled. The peak lists were searched against the sequences as well
750 as the reversed sequences (as decoy) of 14 OCCM subunits using Xi software (ERI, Edinburgh)
751 for identification of cross-linked peptides. Search parameters were as follows: MS accuracy, 6
752 ppm; MS2 accuracy, 20 ppm; enzyme, trypsin; specificity, fully tryptic; allowed number of
753 missed cleavages, four; cross-linker, BS3; fixed modifications, carbamidomethylation on
754 cysteine; variable modifications, oxidation on methionine, modifications by BS3 that are
755 hydrolyzed or amidated on the other end. The reaction specificity for BS3 was assumed to be for

756 lysine, serine, threonine, tyrosine and protein N-termini. For acquisitions where CID and HCD
757 fragmentations were applied (acquisition 1.3.4.6.7 and 9), only b- and y-ions were considered for
758 the fragment ion matches; while for data acquired using a combined fragmentation of ETD and
759 CID or HCD (acquisition 2,5 and 8), b-, y-, c-ions and z-ions were considered for fragment ion
760 matches. Two independent quality control approaches have been applied for identified cross-
761 linked peptide candidates. All cross-linked peptides with estimated 5% FDR at residue pair level
762 were accepted for further structural interpretation. We also accepted cross-linked peptides
763 identified with MS2 spectra that passed machine-learning based auto-validation.

764

765 **In vitro pulldown of Cdt1 with Mcm2-7 proteins**

766 Baculoviruses expressing Mcm2-7 subunits (the Mcm3 was tagged with HA at the N-terminus)
767 and Strep-Strep-SUMO-Cdt1 were prepared in the Profold-C1 expression vector (AB Vector,
768 San Diego). 2.5×10^7 Hi-Five insect cells were infected at a multiplicity of infection of 10 with
769 each MCM subunit alone or in combination with SSS-Cdt1, and harvested at 55 hours post
770 infection. After washing cells in cold PBS, they were placed for 10 minutes on ice in < 1 ml of
771 hypotonic buffer (25 mM Hepes-KOH pH 7.5, 20 mM K glutamate, 1 mM Mg acetate, 1 mM
772 DTT, 5 mM ATP, Protease Inhibitor (Roche, 1 tablet in 50 ml). Cell extracts were prepared by
773 Dounce B homogenization and centrifugal clarification (10,000 rpm in Sorvall SS34 rotor),
774 then 100 μ l of supernatant was incubated of 2 hours on ice with 50 μ l of Strep-Tactin sepharose
775 (IBA) that had previously been washed in PBS and hypotonic buffer. Beads were washed (3 x 5
776 minutes) with IP buffer (25 mM Hepes-KOH pH 7.5, 300 mM KGlutamate, 10 mM MgAcetate,
777 0.04% NP40, 1 mM DTT, 5 mM ATP and protease inhibitor). Bead bound proteins were run on
778 a SDS-PAGE gel and stained with silver.

779

780

781 **METHOD SECTION REFERENCES**

782

783

784

785

786

787

788

789

790

791

792

793

794

795

796

797

798

799

800

801

802

803

804

805

806

807

808

809

810

811

812

813

814

815

816

817

818

819

820

821

822

823

56. Li, X. et al. Electron counting and beam-induced motion correction enable near-atomic-resolution single-particle cryo-EM. *Nat Methods* **10**, 584-90 (2013).
57. Rohou, A. & Grigorieff, N. CTFFIND4: Fast and accurate defocus estimation from electron micrographs. *J Struct Biol* **192**, 216-21 (2015).
58. Scheres, S.H. Semi-automated selection of cryo-EM particles in RELION-1.3. *J Struct Biol* **189**, 114-22 (2015).
59. Biasini, M. et al. SWISS-MODEL: modelling protein tertiary and quaternary structure using evolutionary information. *Nucleic acids research*, W252-258 (2014).
60. Emsley, P. & Cowtan, K. Coot: model-building tools for molecular graphics. *Acta Crystallogr D Biol Crystallogr* **60**, 2126-32 (2004).
61. Pettersen, E.F. et al. UCSF Chimera--a visualization system for exploratory research and analysis. *J Comput Chem* **25**, 1605-12 (2004).
62. Li, W., Zhang, T. & Ding, J. Molecular basis for the substrate specificity and catalytic mechanism of thymine-7-hydroxylase in fungi. *Nucleic acids research*, 10026-10038 (2015).
63. De Marco, V. et al. Quaternary structure of the human Cdt1-Geminin complex regulates DNA replication licensing. *Proceedings of the National Academy of Sciences* **106**, 19807-19812 (2009).
64. Doyle, J.M., Gao, J., Wang, J., Yang, M. & Potts, P.R. MAGE-RING protein complexes comprise a family of E3 ubiquitin ligases. *Molecular cell* **39**, 963-974 (2010).
65. Wiedemann, C. et al. Structure and regulatory role of the C-terminal winged helix domain of the archaeal minichromosome maintenance complex. *Nucleic acids research* **43**, 2958-2967 (2015).
66. Afonine, P.V. et al. Towards automated crystallographic structure refinement with phenix.refine. *Acta Crystallogr D Biol Crystallogr* **68**, 352-67 (2012).
67. Adams, P.D. et al. PHENIX: a comprehensive Python-based system for macromolecular structure solution. *Acta Crystallogr D Biol Crystallogr* **66**, 213-21 (2010).
68. Chen, V.B. et al. MolProbity: all-atom structure validation for macromolecular crystallography. *Acta Crystallogr D Biol Crystallogr* **66**, 12-21 (2010).
69. Amunts, A. et al. Structure of the yeast mitochondrial large ribosomal subunit. *Science* **343**, 1485-9 (2014).
70. Rappsilber, J., Mann, M. & Ishihama, Y. Protocol for micro-purification, enrichment, pre-fractionation and storage of peptides for proteomics using StageTips. *Nat Protoc* **2**, 1896-906 (2007).
71. Chen, Z.A. et al. Architecture of the RNA polymerase II-TFIIF complex revealed by cross-linking and mass spectrometry. *EMBO J* **29**, 717-26 (2010).
72. Cox, J. & Mann, M. MaxQuant enables high peptide identification rates, individualized p.p.b.-range mass accuracies and proteome-wide protein quantification. *Nat Biotechnol* **26**, 1367-72 (2008).